Aerodynamic Investigation of a Composite Low-Speed Fan for UHBR Application

Martin Rodrigues, Laurent Soulat, Benoit Paoletti, Xavier Ottavy, Christoph Brandstetter

To cite this version:

Martin Rodrigues, Laurent Soulat, Benoit Paoletti, Xavier Ottavy, Christoph Brandstetter. Aerodynamic Investigation of a Composite Low-Speed Fan for UHBR Application. Journal of Turbomachinery, 2021, 143 (10), ⟨10.1115/1.4050671⟩. ⟨hal-03440952⟩

Martin Rodrigues
Department of Research and Technology,
Safran Aircraft Engines,
Moissy Cramayel F-77550, France;
École Centrale de Lyon,
University Claude Bernard lyon I,
CNRS, LMFA, UMR 5509,
ECULLY F-69134, France
e-mail: martin.rodrigues@ec-lyon.fr

Laurent Soulat
Department of Research and Technology,
Safran Aircraft Engines,
Moissy Cramayel F-77550, France
e-mail: laurent.soulat@safrangroup.com

Benoit Paoletti
École Centrale de Lyon,
University Claude Bernard lyon I,
CNRS, LMFA, UMR 5509,
ECULLY, F-69134, France
e-mail: benoit.paoletti@ec-lyon.fr

Xavier Ottavy
École Centrale de Lyon,
University Claude Bernard lyon I,
CNRS, LMFA, UMR 5509,
ECULLY F-69134, France
e-mail: xavier.ottavy@ec-lyon.fr

Christoph Brandstetter
École Centrale de Lyon,
University Claude Bernard lyon I,
CNRS, LMFA, UMR 5509,
ECULLY F-69134, France
e-mail: christoph.brandstetter@ec-lyon.fr

Aerodynamic Investigation of a Composite Low-Speed Fan for UHBR Application

A composite fan stage representative of a modern Ultra High Bypass Ratio (UHBR) architecture has been investigated experimentally on a novel test facility at Ecole Centrale de Lyon. These measurements show indications for strong overloading of the tip region resulting in extensive blockage of the blade passage. The performance of the fan is analyzed with extensive instrumentation including radial profiles upstream and downstream of the rotor. Unsteady pressure measurements help to interpret the flow structure in the tip region. The results are presented across a range of operating points on the design speedline. At the stability limit, the machine suffers from non-synchronous vibrations, which result from small-scale aerodynamic disturbances propagating between the leading edges. Detailed analysis of the occurring waveforms is presented for two operating speeds. In order to further analyze the observed phenomena, a numerical study has been conducted using the Reynolds-averaged Navier–Stokes (RANS) solver elsA. The results of steady calculations are discussed in comparison with the detailed experiments. Unsteady simulations near the stability limit accurately predict the aerodynamic disturbances observed during non-synchronous vibrations (NSV). The obtained results are unusual for typical state-of-the-art transonic fans, as they show the same behavior as high-pressure compressor front stages, dominated by a blockage caused by tip-leakage flow. Even though flutter is not observed, the observed non-synchronous vibration mechanism is a critical aeroelastic phenomenon which is of great interest for future designs of low-speed fans.

[DOI: 10.1115/1.4050671]

Keywords: UHBR fan, aeroelastic phenomenon, experimental investigation, high loading, tip-leakage flow, non-synchronous vibrations

Introduction

In order to face the escalating air traffic demands, engine manufacturers have been trying to achieve higher thermal efficiency while reducing noise emissions. The ultrahigh bypass ratio (UHBR) [1,2] fan stands as a promising near-term solution permitting the desired improvements. Increasing the bypass ratio while reducing the fan pressure ratio is essential to increase efficiency. This translates into a rise in the fan diameter and a reduction of the fan rotation speed achieved by placing a gearbox between the fan and the low-pressure turbine stage. The induced weight introduced by the latter is partly counterbalanced by the use of novel composite, slender fan blades. However, the consequent application of modern architectures imposes technological challenges which require intensive research to enable robust designs.

The low fan pressure ratio induces a drift of the take-off working line relative to cruise, thus making the fan operate near its stability limit at low speeds [3]. Stepping out of the current-state-of-the-art architectures, next-generation UHBR fans pose new challenges in understanding design-induced flow phenomena which are difficult to predict at off-design conditions. Particularly due to a complex flow structure in the rotor section evolving at off-design conditions, the prediction of respective phenomena is still inaccurate. Highly three-dimensional flows such as compression shocks, boundary layer interaction, and tip-leakage flow impose enormous challenges toward the used simulation methods, specifically concerning turbulence modeling.

For modern lightweight structures, aeroelastic and aeroacoustic interaction mechanisms with the complex flow structures increasingly lead to critical conditions and limit the operating range before the onset of rotating stall. It is not possible anymore to study aerodynamic phenomena independently from those interaction mechanisms, which greatly depend on the flow structure in the tip region. The known aeroelastic instability mechanisms which limit the operating range of fans and compressors comprise self-excited mechanisms (Flutter) as well as so-called non-synchronous vibrations (NSV), resulting from a lock-in between an aerodynamic excitation phenomenon with a structural vibration pattern. While the fundamental understanding of the causes for flutter has been improved throughout the past decades and allowed to develop efficient countermeasures like intentional mistuning (i.e., Ref. [4]), the causes for NSV are still under discussion in the literature. Concerning typical fan flutter (part-speed flutter bite), the dominant mechanism is an acoustic resonance between a structural vibration pattern and acoustic modes, which are reflected in the intake [5]. The critical modes comprise forward traveling patterns of low circumferential wave number, which are propagative only in the upstream direction and cutoff due to the rising swirl downstream of the fan. Hence, only a narrow range

---

Contributed by the International Gas Turbine Institute (IGTI) of ASME for publication in the Journal of Turbomachinery. Manuscript received December 8, 2020; final manuscript received February 23, 2021; published online May 12, 2021. Tech. Editor: David G. Bogard.

of modes fulfill this condition and can be well predicted. Through the intentional design of the fan blades, the sensitivity toward this mechanism can be significantly reduced [6].

Non-synchronous vibration instead develops due to circumferentially convected aerodynamic disturbances [7,8] which randomly excite blade vibration modes. Due to a phase lock-in Ref. [9] mechanism with a structural vibration pattern, a spatial organization of the aerodynamic disturbances can develop and enforce a self-sustaining mechanism. This phenomenon has been described in several cases in the literature concerning typically front stages of core compressors [10]. It is well known that the blockage in the tip region caused by the tip-leakage flow is a governing factor for the convective transport phenomenon to occur. While the described phenomena have been intensively studied on high-speed fans and core compressors, the knowledge concerning modern low-speed fan architectures is very limited and representative experimental studies are necessary [11].

To overcome this situation, a comprehensive investigation of composite material, low-pressure ratio fan has been carried out with a focus on both the aerodynamic behavior and aeroelastic interaction mechanisms. The fan stage, developed by Safran Aircraft Engines within the European project ENOVAL (European Unions Seventh Framework Programme for research, technological development, and demonstration, grant agreement no 604999) is representative of geometry for state-of-the-art UHBR configurations. A scaled model was investigated at representative conditions at a novel fan-test facility at Ecole Centrale de Lyon, using extensive instrumentation. The results of the experimental investigation are presented in comparison with numerical simulations. To the authors' knowledge, this study presents the first comprehensive investigation on the aeroelastic behavior of a composite low-speed fan. As will be shown, the results concerning the observed instability mechanism are highly surprising due to their resemblance with the behavior of high-speed compressors. The study is structured as follows:

- The experimental and numerical setup as well as the used methods is introduced
- Experimental results in the stable operating range are presented and discussed in comparison with numerical simulations
- Results of transient experiments at the limit of the operating range are analyzed with a focus on aeroelastic interactions
- A discussion of the observed phenomena is given, accompanied by results of unsteady simulations

Test Facility ECL-B3

The test facility ECL-B3 stands as an innovative, novel, multi-physical test rig designed and built in cooperation between Ecole Centrale de Lyon and Safran Aircraft Engines through the ANR-EQUIPEX program. This test rig is designed to host fan architectures representative of modern UHBR stages at scales between 1:4 and 1:3 [12]. The tested vehicle in this study was designed by Safran AE and is a technology demonstrator of a next-generation UHBR stage. The test rig only contains the bypass stream consisting of a composite, low-speed transonic fan and outlet guide vanes (OGV). The latter have been designed specifically for this rig (extension of the blades' foot region does not exist in the real engine) to provide the rotor with representative exit conditions. This study ensues a test campaign that characterized the vehicle within the ENOVAL European project.

Test Setup. The ECL-B3 test rig presented in Fig. 1(*a*) was specifically built to ensure disturbance-free inflow conditions enabling highly accurate aerodynamic and acoustic characterization of the vehicle, operated in an open cycle [12]. After traversing rows of silencers, the air enters an anechoic chamber and is sucked into the core through a turbulence control screen (TCS). The air subsequently flows into an axisymmetric coned-shaped throttle controlling the mass flow. The air exits through an exhaust system consisting of a 25-m-long circular pipe including a Venturi nozzle for precise measurement of the massflow. The air is eventually extracted to the atmosphere through final rows of silencers. The machine room, acoustically isolated from the test room, hosts a 3-MW electric motor allowing a rotation speed of approximately 16,000 rpm. A torquemeter is mounted between the fan shaft and the gearbox shaft enabling an accurate measurement of the applied power. The machine core schematized in Fig. 1(*b*) was designed in a modular fashion granting a time-efficient and flexible change of test configuration. It also facilitates the application of instrumentation, as multiple accesses are available for traversable instrumentation around the circumference.

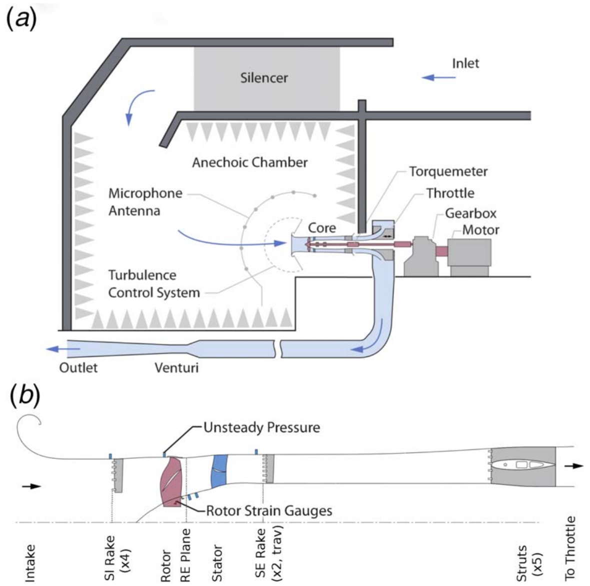

Fig. 1 Schematic view of (*a*) ECL-B3 test facility and (*b*) machine core detail

Instrumentation. The acquisition system allows more than 800 signals to be recorded simultaneously. The machine core is instrumented with pressure and temperature sensors distributed from the bellmouth-shaped intake to the throttle mechanism at various meridian positions, on the hub and casing. Microphone sensor arrays are mounted in the vicinity of the stage and a rotatable mobile antenna upstream of the TCS.

The ENOVAL aerodynamic test campaign consisted of two maneuvers: the fan mapping measurements, with full traversals of the stage exit plane at stable operating conditions, and the operability measurements during which the machine was throttled toward the stability limit. During the fan mapping, the machine was instrumented with three distinct sets of rakes to measure the stage performance, as depicted in Fig. 1(*b*). The stage inlet (SI) plane and stage exit (SE) plane are instrumented, respectively, by four fixed rakes and two circumferentially traversable rakes. Five radial struts are located downstream of the stage. The rakes and struts are all instrumented by pressure and temperature probes. During the operability measurements, the SI and SE rakes were removed. The stage performance was measured using the instrumented struts. During each maneuver, a total of 17 miniature, high-frequency response pressure transducers were mounted on a removable block on the casing over the tip of the fan blade in order to measure space- and time-resolved unsteady wall pressure above the rotor. The measurement of structural vibrations was implemented through strain gauges on rotor blades, transferred via telemetry. The main parameters of the investigated fan stage are summarized in Table 1.

This study also provides results from pneumatic probe measurements, performed simultaneously upstream and downstream the

Table 1 Main parameters of UHBR fan stage

Outer casing diameter	508 mm (20″)
Rotor number of blades	16
Stator number of blades	36
ADP blade tip speed	280–340 m/s
ADP tip Mach number	>1.3
ADP tip gap size	≈0.8% tip chord

rotor. The rotor inlet plane corresponds to the stage inlet (SI) plane, the rotor exit (RE) plane is located 0.4 rotor chord downstream of the fan. Radial measurements are carried out by means of miniature cobra-type five-hole pressure probes and PT100 resistance thermometers measuring total temperature. The head diameters are 0.9 mm and 2.5 mm, respectively. Each measurement plane is instrumented with two probes of a kind. The probes are traversed in the radial direction, and the probe yaw was adjusted at each radial position to align with the local flow direction behind the rotor. A total of 30 radial positions were evaluated in both planes. The calibration and post-processing procedures used are described in Ref. [13].

Computational Method. The elsA solver [14] developed by Onera is used to perform three-dimensional (3D) Reynolds-averaged Navier–Stokes (RANS) and time-resolved RANS (URANS) simulations. A first-order accurate time integration scheme is used. Two turbulence models are studied: the Smith model [15], selected as it is commonly used in industrial numerical procedures and the $k-\omega$ model with the KoK formulation [16].

Steady Case. Boundary conditions for steady simulations consist in prescribing total pressure, total enthalpy, velocity direction, and primitive turbulent quantities (k or l) at the inlet. The direction of injection is specified as normal to the cells' surface. A radial equilibrium with a static pressure value at the pivot point is prescribed at the outlet. Interfaces between stationary and rotating domains are modeled as mixing planes.

Unsteady Case. A method inspired by the work from [17–20] was implemented for the URANS calculations. The outlet boundary is modeled by a choked nozzle whose section is adjusted to control the reduced massflow for each operating point (OP). The purpose of this approach is to avoid prescribing a static pressure value at the outlet boundary condition which can be limiting for the study of operating points near the stall boundary. The $k-\omega$ turbulence model was used for the unsteady calculations due to a better agreement with the experimental results for highly loaded operating points as will be discussed later.

Geometry Description. The calculation domain for RANS calculation is a single passage configuration of the studied stage as shown in Fig. 2. The struts being far behind are not taken into account in this study. The fan inlet is placed approximately 20 rotor chords upstream of the fan. The outlet is located at seven stator chords downstream of the OGV row. A low Reynolds structured mesh is generated with an O–H mesh topology around the blade, and a value of $y^+ < 1$ is set throughout the whole domain. Around 100 nodes are located along the blade chord and 120 nodes along the span including 35 nodes in the tip gap region. A mesh sensibility study yielded a mesh with approximately 6×10^6 mesh nodes per passage: 3.5 in the rotor, 1.5 in the stator, and 1.0 in the intake domain. A view of the mesh detail around the rotor blade is included in Fig. 3. The intake domain was considered to account for changes in the boundary layer evolution with the operating point.

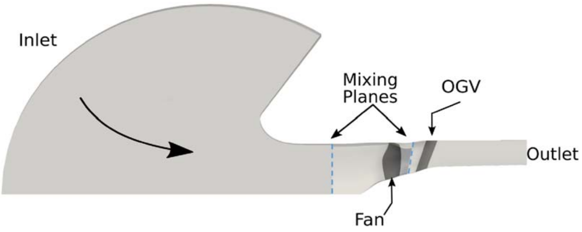

Fig. 2 Computational domain for single passage calculation

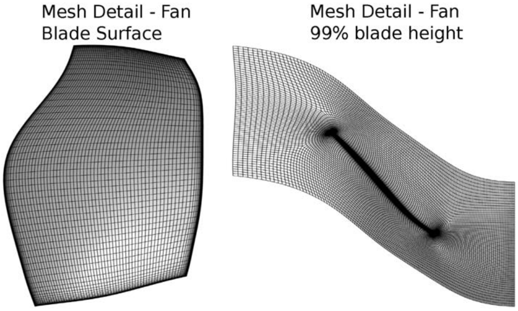

Fig. 3 View of the mesh around the rotor blade

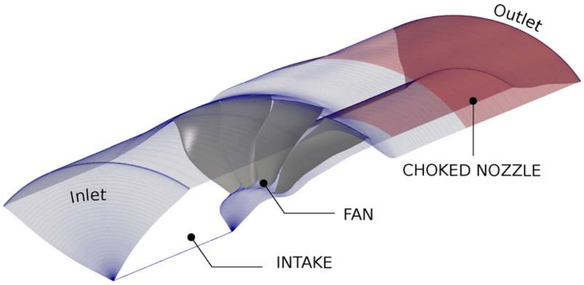

Fig. 4 Computational domain (four rotor passages) for URANS calculation

The domain for URANS calculation consists in four rotor blade passages with around 2×10^6 points per passage. The OGV row was not included in this setup, and the inlet domain was shortened. The inlet boundary condition is approximately located at 7.5 rotor chords upstream of the fan. A duplicated view of the four rotor blade passages is provided in Fig. 4. A first calculation was performed by simply adding a choked nozzle to the steady calculation domain. This calculation served as a validation that the performance and flow features were similar for a stable operating point. An operating point near the stability limit was obtained with this configuration and has served as a restart point for the URANS calculation.

Steady Results in Stable Operating Range

This section introduces the results obtained from the different measurement campaigns for the design speedline. The RANS performance is validated against experimental performance, and results suggest an overall good prediction. For loaded operating conditions, differences arise depending on the choice of turbulence model. Results are detailed in the following paragraphs.

Fan Performance map. The stage performance map for the design speedline N100 is presented in Fig. 5. Experimental data from both fan mapping and probe measurements are compared to RANS simulations. The results indicate the following:

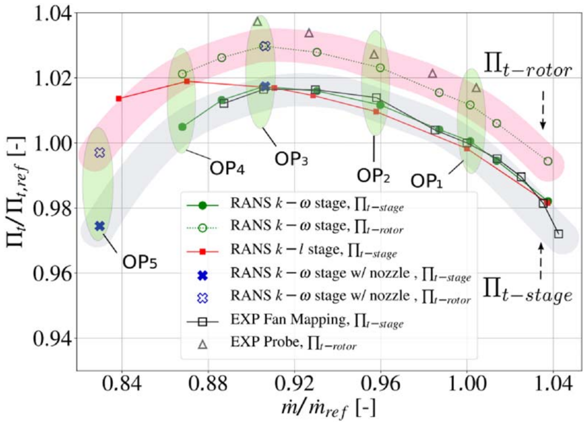

Fig. 5 Fan performance map at design speedline N100

- The long and flat performance characteristic exhibits a significant drop in total pressure ratio toward loaded operating points. The rotor pressure ratio evolution extracted from the stage simulations manifests the same trend, thus indicating that the deterioration of performance mainly originates from the rotor. For this reason, this study will only focus on the rotor behavior.
- The prediction of performance is strongly affected by the choice of turbulence model. While the $k-\omega$ model well predicts this drop, the $k-l$ model seems to attenuate the rotor losses, thus extending the maximum pressure ratio point. This particular point will be discussed in the section “Influence of Turbulence Modeling.” Note that only the experimental results from fan mapping for stabilized points are shown and are not representative of the whole operating range (as introduced in the “Highly Loaded Conditions” section).
- Performance measured by probes is in coarse agreement with RANS prediction. Due to safety reasons, probe measurements could only be carried out from OP1 to OP3, not covering the pressure ratio drop. Nevertheless, profiles seem to provide indications of an onset of a rotor tip overloading.

Radial Profiles. Normalized total pressure (*Pt*) and total temperature (*Tt*) profiles at the RE plane plotted against normalized duct height (*h*) are gathered in Fig. 6. The 30 radial measurement positions are visible on the right-hand side of the graphs. Five profiles corresponding to operating points ranging from OP1 to OP3 are presented (comp. Figure 5). The miniature probes enable us to study the flow structure with high levels of refinement. What can be observed from Fig. 6 is that when throttled, the total pressure profiles slowly increase between 0 and 50%*h*. For operating points near OP3, a dent in the *Pt* profile begins to appear at 95%*h* due to the evolution of tip blockage related to the tip-leakage flow. The total temperature profiles indicate that the increase of work is concentrated in the tip region (80–100% *h*) while the 0–80% *h* region witnesses an almost constant work independent of the throttle position.

Figure 7 presents the validation of RANS $k-\omega$ profiles against experimental profiles at the RE stage for OP1, OP2, and OP3. On the left-hand side, the rotor total pressure ratio Πt, rotor is plotted against normalized duct height *h*. The prediction is in good agreement in the 0–80% *h* region. However, the RANS prediction is noticeably degraded in the 80–100% *h* region and a difference of order 3% arises between the pressure ratio values at 98% *h* at OP3. The right-hand-side graph shows the total temperature difference ΔTt, rotor. A good prediction is ensured by RANS in the 0–80% *h* region. However, the RANS simulation seems to confine the rotor work to a region closer to the casing than what is observed by the experiment. Several factors can cause the observed discrepancies:

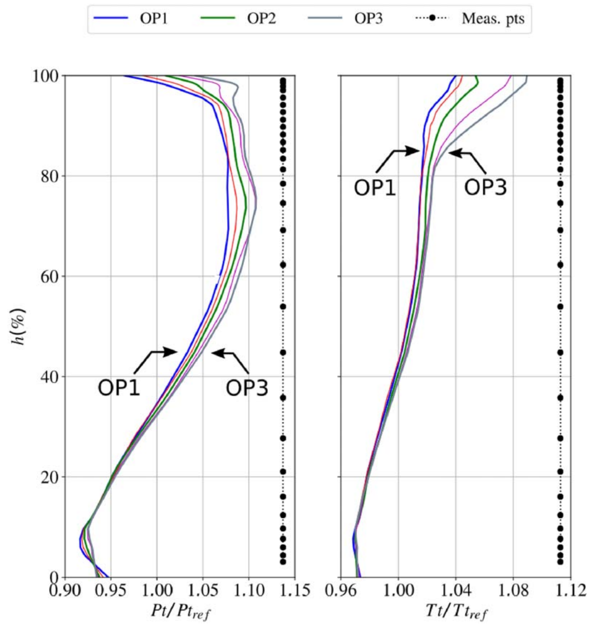

Fig. 6 Experimental *Pt* (left) and *Tt* (right) profiles at ROTOR exit plane at OP ranging from OP1 to OP3

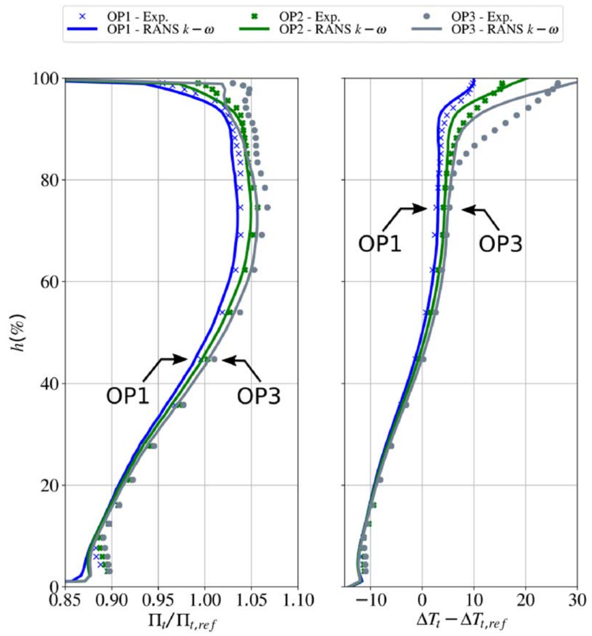

Fig. 7 Experimental Πt (left) and ΔTt (right) profiles for rotor only at OP ranging from OP1 to OP3 compared with RANS

- Blade geometry: for practical reasons, the simple method is to calculate the blade running geometry for one rotation speed and one reference operating, point thus yielding a constant geometry blade along the characteristic. Indeed, a better representativeness would be ensured by the calculation of one running geometry per investigated operating point.
- Simplification on geometry: the single passage configuration restricts the study to uniform blade tip gap size and stagger angle in the rotor. Variabilities in tip gap size within a range of 0.15% tip chord and stagger were observed during tests which is obviously not accounted for in RANS simulations. Nonlinear effects due to non-periodic tip gap sizes and blade

stagger angles on the local flow structures (and globally on performance) are expected to play a crucial role in the representativeness of the simulations [21]. These variabilities intensify with blade deterioration and manufacturing tolerance.

- RANS modeling: it is known that the behavior of the tip-leakage flow can become highly unsteady [22], the interaction between the tip-leakage flow, the shock, and the boundary layer developing downstream is particularly poorly predicted at off-design conditions. The observed tip flow features highly resemble those of high-pressure compressors undergoing vortex breakdown in the tip region resulting in low momentum fluid inducing blockage [22,23], which imposes systematical problems for RANS approaches. This has motivated a preliminary URANS study which will be described subsequently.

Influence of Turbulence Modeling. As shown in Fig. 5, turbulence modeling strikingly influences the evolution of the performance characteristic for loaded conditions. While the simulation results for the range between OP1 and OP3 are independent of the turbulence model, significant differences arise for OP4. A side-by-side comparison between the used turbulence models is shown in Fig. 8 on a blade-to-blade view at 99%h contoured by turbulent kinetic energy (TKE). What is remarkable is that the $k-l$ model yields more energetic turbulent structures originating from the tip-leakage flow than the $k-\omega$ model. These structures are confined near the blade suction side and casing in the passage with the $k-l$ model as opposed to the $k-\omega$ model predicting more diffuse structures causing a larger blockage in the tip region. The shock position does not seem strongly affected by the turbulence model in this case. What is more, the prediction of the $k-\omega$ model is closer to experimental data, regarding both the performance characteristic and the radial profiles and the wall pressure signature above the rotor, which will be discussed in the section "Highly Loaded Conditions."

The systematic change of the flow topology around OP4 is well depicted in the visualization of the surface streamlines in Fig. 9. This illustration shows that separated flow occurs downstream of the shock. When throttling, separated flow is indicated by the appearance of a saddle point type critical point. Also, for the operating point OP5, the whole tip region runs subsonic and shows highly complex traces of flow separation (saddle point and focus-type critical points). All of which indicate that the flow in the tip region dominates the behavior of the fan at highly loaded conditions. The results suggest that the prediction of the steady performance is strongly influenced by the chosen turbulence model ($k-l$, $k-\omega$), specifically concerning the region affected by the tip-leakage flow. This point is of particular importance regarding the instability behavior analyzed in the following section.

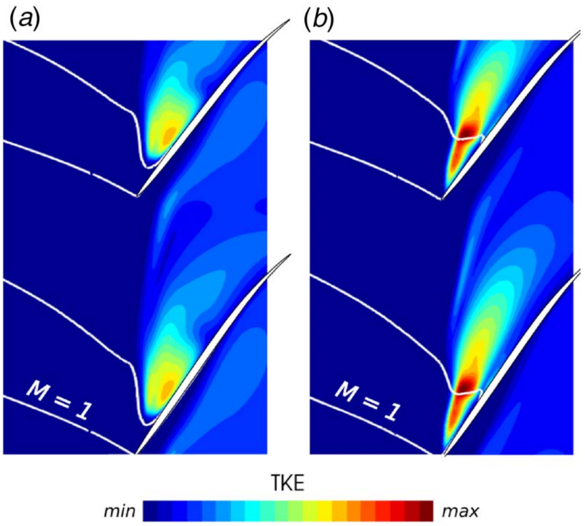

Fig. 8 Blade-to-blade view at 99%h contoured by turbulent kinetic energy with $M=1$ isocontour line at OP4: (a) $k-\omega$ and (b) $k-l$ models

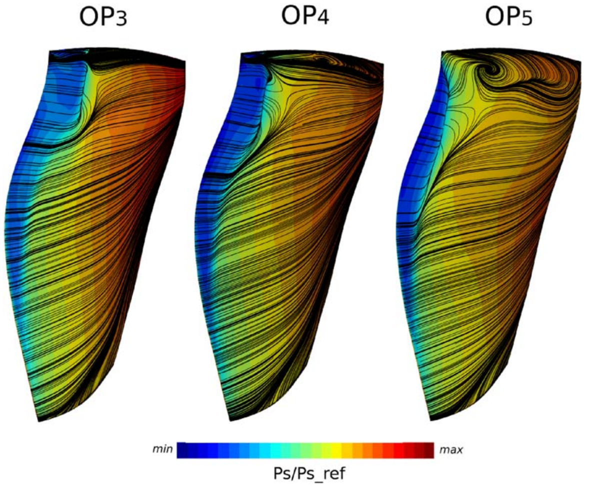

Fig. 9 Fan suction side streamlines for OP3, OP4, and OP5 contoured by norm. Static pressure: $k-\omega$ RANS simulation.

Highly Loaded Conditions

The fan characteristic including highly loaded operating points is presented in Fig. 10, comparing experimental and numerical results. It can be observed that the operating range of the fan extends far beyond the last operating point that was investigated during the fan mapping (between OP3 and OP4). Until OP4, the RANS prediction of the fan performance is adequate. For OP5, the measured pressure ratio of the stage lies significantly above the simulation, which could not be throttled further due to convergence issues. The rotor-only simulation with a choked nozzle at OP5 coincides with the measured stage pressure ratio, indicating that the predicted losses exceed the experimental results.

Unsteady wall pressure measurements above the rotor have been carried out, using an array of Kulite sensors. The ensemble average of those measurements for the operating points OP2 through OP6 is presented in Fig. 11(a). Clearly, a continuous detachment of the shock from the blades leading edge can be derived. Regarding the unsteadiness of the flow field near the casing observed for these operating points, Fig. 11(b) draws a clear picture by showing the

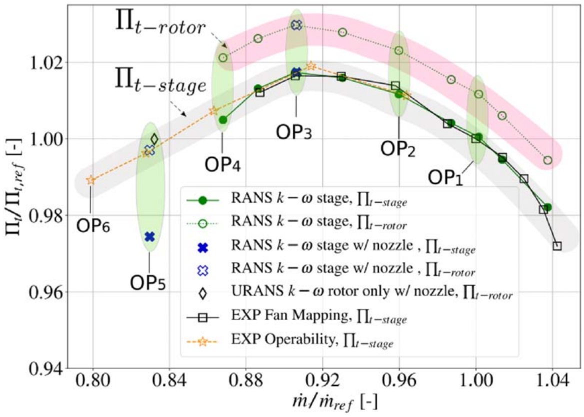

Fig. 10 Fan characteristic, comparison of steady fan mapping experiment results, operability experiment results, and $k-\omega$ RANS and URANS simulations

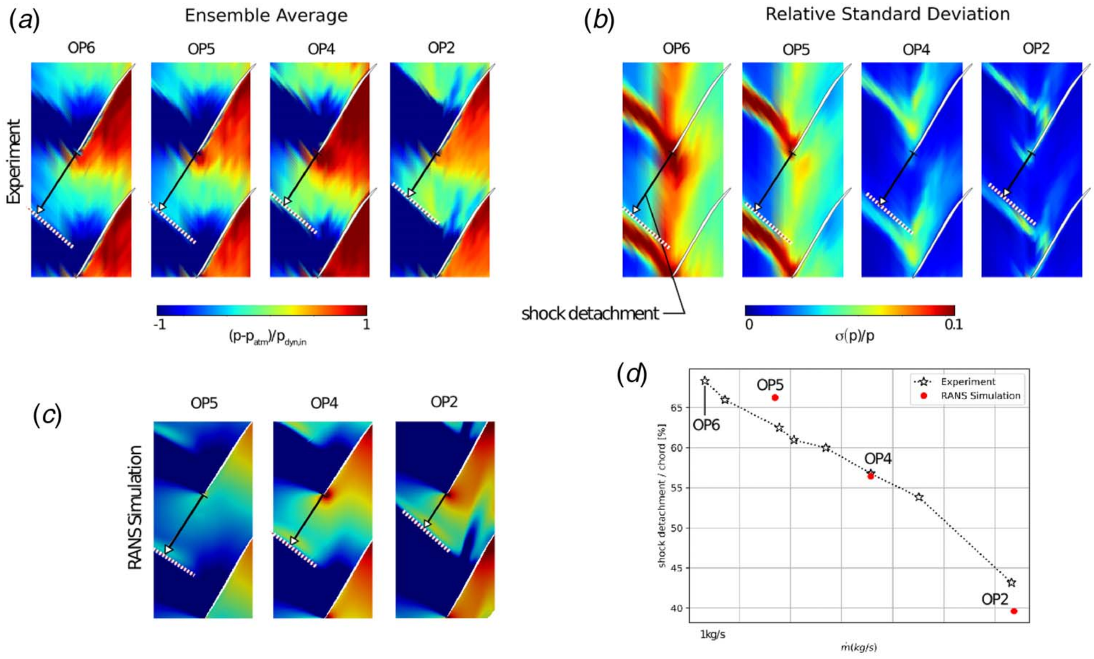

Fig. 11 Shock detachment comparison between EXP and RANS for 4 operating points: (*a*) ensemble average of wall static pressure, (*b*) locations where fluctuation of wall static pressure exceeds inlet dynamic pressure, (*c*) RANS simulation shock detachment, and (*d*) linear evolution of shock detachment EXP versus computational fluid dynamics (CFD)

relative standard deviation of the measured wall pressure. At OP2, only weak fluctuations of the shock are observed. For OP4, those shock fluctuations become more intense, and likewise, a zone of unsteadiness emerges downstream of the shock in the area where the tip-leakage flow mixes with the main flow. While further throttling toward OP5 and OP6, this zone intensifies and inclines toward the leading edge of the trailing blade.

A comparison of the wall pressure contour with the steady simulations ($k-\omega$) is presented in Fig. 11(*c*). For OP2 and OP4, the pressure level and shock structure are in good agreement with the measurement shown in Fig. 11(*a*). The distortion due to the tip-leakage flow is well represented as well. At OP5, the position of the shock is still comparable to the experiment; however, the pressure gradient in the downstream part is less intense in the simulations, which is coherent with the results of the performance characteristic in Fig. 10. Regarding the detachment of the shock in the chordwise direction from the leading edge, presented in Fig. 11(*d*), the agreement between experiment and simulation is still accurate within a range of 5% chord for OP5. Hence, the simulation at OP5 seems to slightly overpredict the detrimental effect of the tip-leakage flow on the overall flow structure in the tip region. However, the general tendency justifies an analysis of unsteady simulations, started from the steady results at OP5.

In a first study to analyze the unsteady flow features developing close to the stability limit, a periodic sector of four rotor blades has been simulated in a rotor-only configuration attached to a convergent nozzle (Fig. 4) for the design speedline N100. As depicted in Fig. 10 the operating point converges toward close to the steady solution. However, in the unsteady simulations, small-scale disturbances visible in the presented fluctuation of the wall pressure signal separate from the leading edges and propagate around the circumference as shown in Fig. 12. The disturbances propagate backward in the relative frame of reference with 40% of the rotor speed; hence, the absolute propagation speed amounts to $0.6\Omega R$. After approximately four rotor revolutions, the simulation reaches a periodically converged state, which is shown in the figures. According to the theory on NSV presented in Refs. [9] and [10], the phase of the individual disturbances can adapt to the blade oscillation phase for high blade vibration amplitudes and affect the number of disturbances depending on the structural nodal diameter while the free propagation speed of the disturbances is dominated by the aerodynamic conditions. It will be shown later that, in the experiment, $|N_a| = 12$ and $|N_a| = 13$ disturbances are observed for the locked-in state. As no blade vibration was imposed in the simulations, the initiation of the disturbances is symmetric and synchronized around the circumference and one disturbance occurs per rotor blade ($|N_a| = N_b = 16$).

The results presented here closely resemble those of the high-speed axial compressor investigated in Ref. [10], where the distortions traveling between the blade leading edges were identified as small radial vortices which were as well responsible for the onset of NSV. The unsteady pressure drop associated with the typical aerodynamic disturbances was identified to be of the order of the inlet dynamic pressure of the main flow (area average of dynamic pressure in the absolute frame of reference at stage inlet). Based on these studies, the unsteady pressure signal was analyzed for locations, where this value was exceeded. The cumulative occurrence is presented in Fig. 13, revealing zones of intense unsteady disturbances.

When comparing the zones of high fluctuation of the wall pressure, a good agreement between the simulations and the experiment is evident. The propagation zone of the disturbances is well captured. In the experiment, the fluctuation of the expansion zone is slightly more pronounced than in the simulation. These results are particularly interesting concerning the transient experimental results, presented in the following.

Unsteady Measurements. Transient measurements have been carried out by continuously throttling the fan stage from a stabilized operating point near the stability limit (OP6) until either a rotating stall was detected or blade vibration amplitudes reached a critical limit. At all investigated speedlines, the machine develops strong non-synchronous activity, observed with both unsteady pressure sensors and strain gauges on the rotor blades. At all speedlines except for N80, the rotating stall was detected after a period of non-synchronous precursors. At speed N80, the experiment was aborted due to high blade vibration on Mode 3. Exemplarily, the results for two speedlines will be presented in the following.

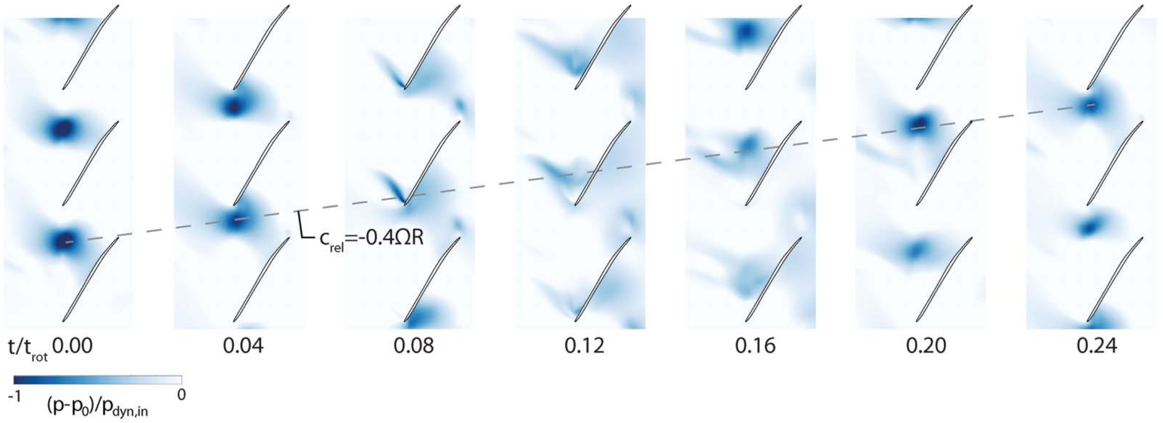

Fig. 12 URANS simulation of unsteady wall static pressure fluctuations; small disturbances separate from the blade leading edge and propagate in the circumferential direction

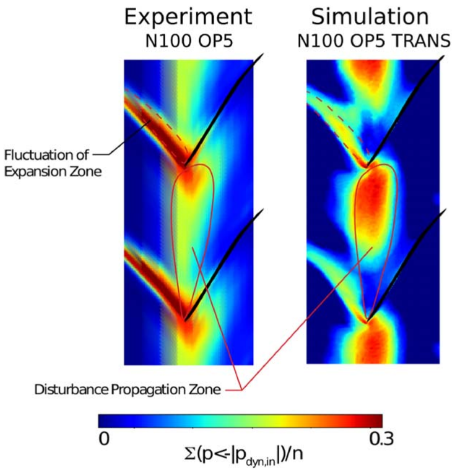

Fig. 13 Cumulation of unsteady pressure exceeding inlet dynamic pressure at OP5

Figure 14(*a*) presents the spectrogram of an unsteady pressure sensor near the leading edge for a measurement at the design speedline N100. The ensemble average of each 10 revolutions has been subtracted to isolate non-synchronous disturbances [24]. Before the onset of rotating stall at revolution 0, a broadband distortion in a frequency range of around half the blade passing frequency (BPF) is present with prominent singular peaks. After the onset of the rotating stall, a dominant peak appears near engine order (EO) 0.5 as well as its modulations with the blade passing frequency at EO16 ± EO 0.5. The averaged spectrogram for the 2000 revolutions before rotating stall is presented in Fig. 14(*b*), clearly revealing the non-synchronous peaks of the pre-stall disturbance, with dominant frequencies at EO7.20, EO7.81, EO8.20, and EO8.80. This type of disturbance, consisting of a broadband "hump" around 50% BPF, is typically described in the literature under the term "rotating instability." Synchronously measured, the spectrogram of a strain gauge on a rotor blade is presented in Fig. 14(*c*). Here, Eigenmodes 1 and 3 of the rotor blades are clearly depicted during the pre-stall phase (blade Eigenmode 2 does not show significant non-synchronous activity and is blanked out for confidentiality reasons). After stall onset, the first mode reaches high amplitudes coherently with the EO0.5 disturbance observed in the pressure spectrum. In order to analyze the circumferential mode order (nodal diameter), redundant strain gauges on multiple rotor blades are analyzed with the method described by Brandstetter et al. in Ref. [24]. The individual signals are band-pass filtered on the respective mode, and by cross-correlating permutations of sensor pairs, the propagation speed of a circumferential mode is determined. The ratio between the engine order of the mode and the determined propagation speed derives the nodal diameter according to

$$\mathrm{ND} = \Omega R \, \frac{\mathrm{EO}_{rel}}{c_{prop,rel}} \tag{1}$$

Based on this method the results for the first Eigenmode are presented in Fig. 15. For the pre-stall phase, no dominant nodal diameter can be identified. After stall onset, clearly a backward-traveling nodal diameter of ND = −3 establishes (in the relative frame of reference). For Mode 2, the figure is omitted since no dominant nodal diameter was derived for this speedline. The results for Mode 3 instead, presented in Fig. 16, show an alternating vibration pattern of forward traveling nodal diameters of ND = 3 and ND = 4 already long before rotating stall. These results are confirmed by synchronous tip-timing measurements. Considering these results, the individual peaks arising in the frequency spectrum can be clearly explained according to the theory on lock-in mechanisms leading to NSV [9]. The frequency of the vibration Mode 3/node diameter (ND)3 in the stationary frame is given as

$$\mathrm{EO}_{stat} = \mathrm{EO}_{rel} + \mathrm{ND} = \mathrm{EO}4.80 + \mathrm{ND}3 = 7.80 \tag{2}$$

Modulation with the rotor blades leads to a frequency of EO8.2 in the stationary frame of reference. This can be associated with an aerodynamic disturbance with a wavenumber of $Na = -13$ (the sign of N_a indicates the propagation direction in the rotor-relative frame of reference), which is in resonance with the structural mode of ND3 according to $\mathrm{ND} = N_b - |N_a|$. In the same way, the two peaks at EO7.20 and EO8.80 can be assigned to the vibration pattern in ND4 which is in resonance with an aerodynamic disturbance of $N_a = -12$. The propagation speed of the aerodynamic disturbance in the stationary frame of reference can be calculated to

$$\frac{c_{prop,|N_a=-13|}}{\Omega R} = \mathrm{EO}8.20/|N_a = -13| = 0.63 \tag{3}$$

$$\frac{c_{prop,|N_a=-12|}}{\Omega R} = \mathrm{EO}7.20/|N_a = -12| = 0.60 \tag{4}$$

It can be seen that both aerodynamic modes propagate with approximately the same speed in the stationary frame of reference. The speed indicates a convective phenomenon, which means that those two modes are not superimposed on each other. Rather, a non-homogeneous distribution of disturbances establishes which alternates its circumferential mode order and propagates with an almost constant speed of approximately 60% ΩR. This disturbance interacts and alternately excites structural vibration patterns based on Mode 3

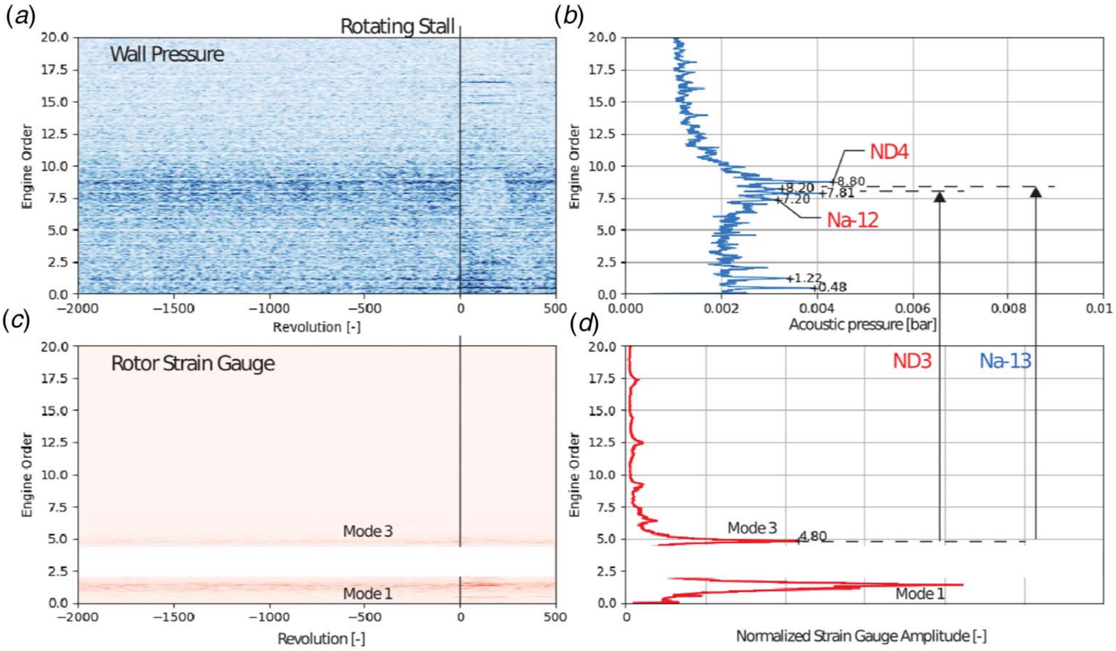

Fig. 14 Wall pressure and strain gauge signal during stall onset at N100: (*a*) and (*b*) wall pressure, (*c*) and (*d*) rotor strain gauge

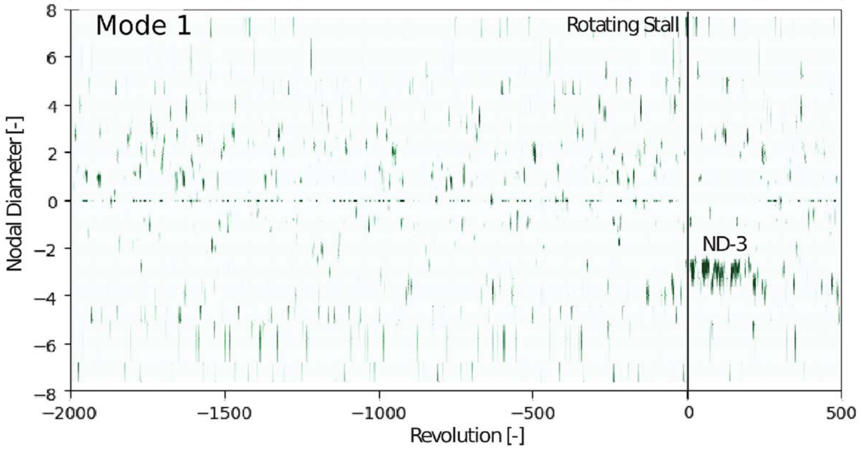

Fig. 15 Dominant nodal diameter during stall onset N100 for mode 1, derived from cross-correlations of strain gauges

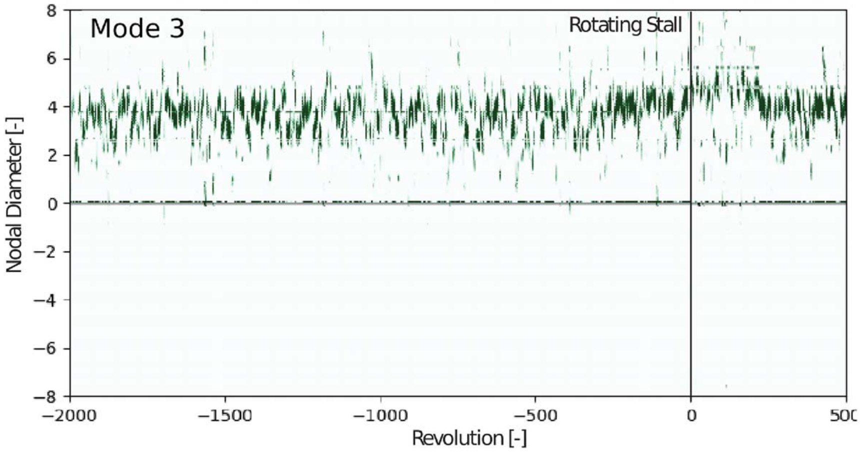

Fig. 16 Dominant nodal diameter during stall onset N100 for mode 3, derived from cross-correlations of strain gauges

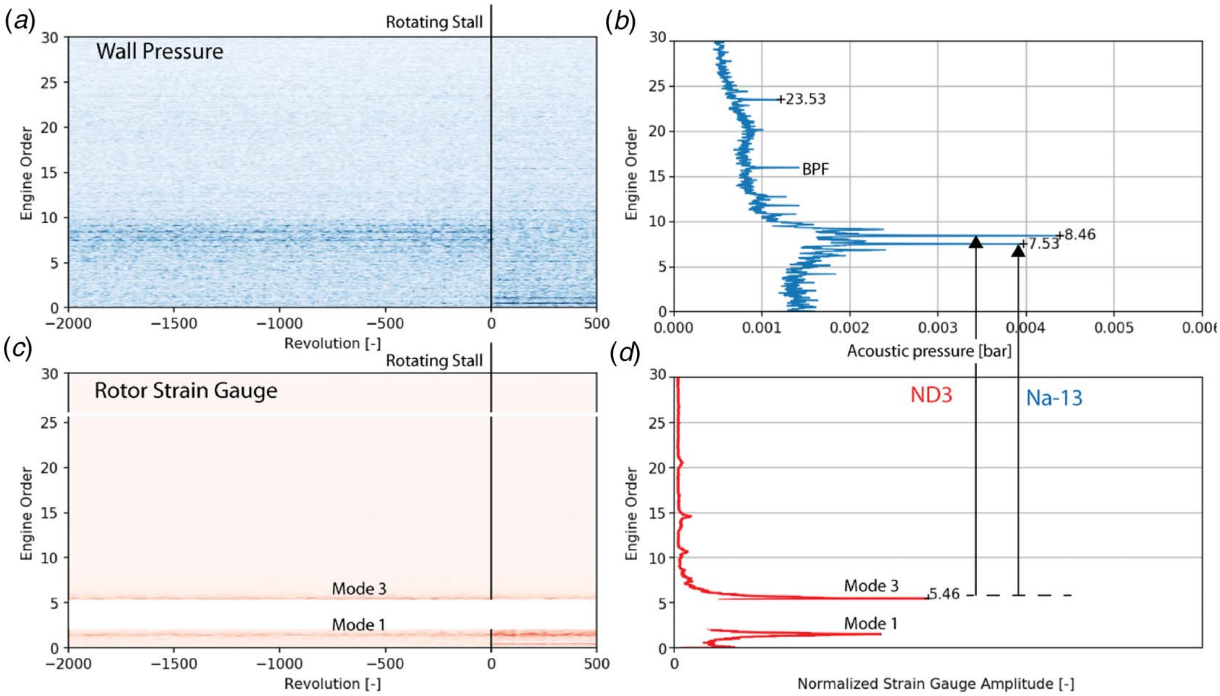

Fig. 17 Wall pressure and strain gauge signal during stall onset at N85: (*a*) and (*b*) wall pressure, (*c*) and (*d*) rotor strain gauge

in circumferential mode orders 3 and 4 and follows a lock-in mechanism. When entering a rotating stall, the machine develops single-stall cells which primarily excite the first structural Mode 1.

Exactly the same phenomenon was observed for part-speed operation but with far more intense amplitude. The wall pressure spectrogram at 85% of the nominal speed is presented in Fig. 17(*a*) and the pre-stall average in 17(*b*) with the corresponding strain gauge measurement in Figs. 17(*c*) and 17(*d*). For this speedline, the measured amplitude of Mode 3 is higher than that during the pre-stall phase at design speed. Likewise, the individual peaks which evolve from the broadband disturbance around EO8 are pronounced more significantly. The dominant peaks at EO8.46 and EO7.53 indicate again a dominant nodal diameter of 3 for Mode 3, interacting with a backward-traveling aerodynamic disturbance of $N_a = -13$. Additionally, the observed peak at EO23.53 confirms the scattering of the aerodynamic disturbance with the rotor blades, representing the positive sideband of the modulation (N_b $+$EO7.53 $=$ EO23.53). The waveforms depicted in Fig. 17 are clearly confirmed when regarding the derived circumferential order for Mode 3, presented in Fig. 18, exposing a dominant nodal diameter of 3 for the whole pre-stall phase. Here, the propagation speed of the disturbance is calculated as $0.58\Omega R$.

Comprising the results for all investigation speedlines between 40% and design speed, Fig. 19(*a*) shows the measured amplitude of Eigenmodes 1 and 3 of the rotor blades during the pre-stall phase. It can be seen that at 80% nominal speed, a maximum is reached for Mode 3. The amplitudes at this speedline reached critical limits during the test. The other eigenmodes do not show this particular behavior. Regarding the dominant mode orders for all speedlines, a widely linear evolution can be derived from

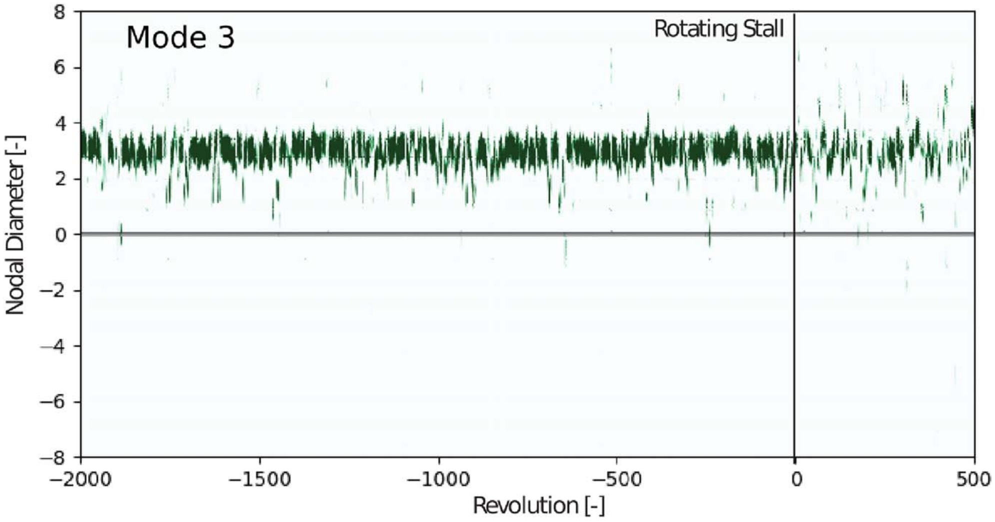

Fig. 18 Dominant nodal diameter during stall onset N85 for mode 3, derived from cross-correlations of strain gauges

Fig. 19(*b*). At N60, a backward-traveling mode with ND2 establishes, corresponding to an aerodynamic disturbance of $N_a = 18$. The wavenumber of the aerodynamic disturbance linearly decreases with rising rotor speed until the described circumferential mode order of $N_a = -12$ and $N_a = -13$ at design speed. In the same manner, the dominant nodal diameter of the vibration pattern increases according to $\mathrm{ND} = N_b - |N_a|$. The evolution of the propagation speed of the aerodynamic disturbances is presented in Fig. 19(*c*), revealing almost constant speed in a narrow range between 54% and 60% of the rotor speed. These results indicate that the principal excitation mechanism does not change throughout all experiments and is dominated by a convective phenomenon with distinctive propagation speed, which is correctly predicted by the unsteady simulations, presented in Fig. 12.

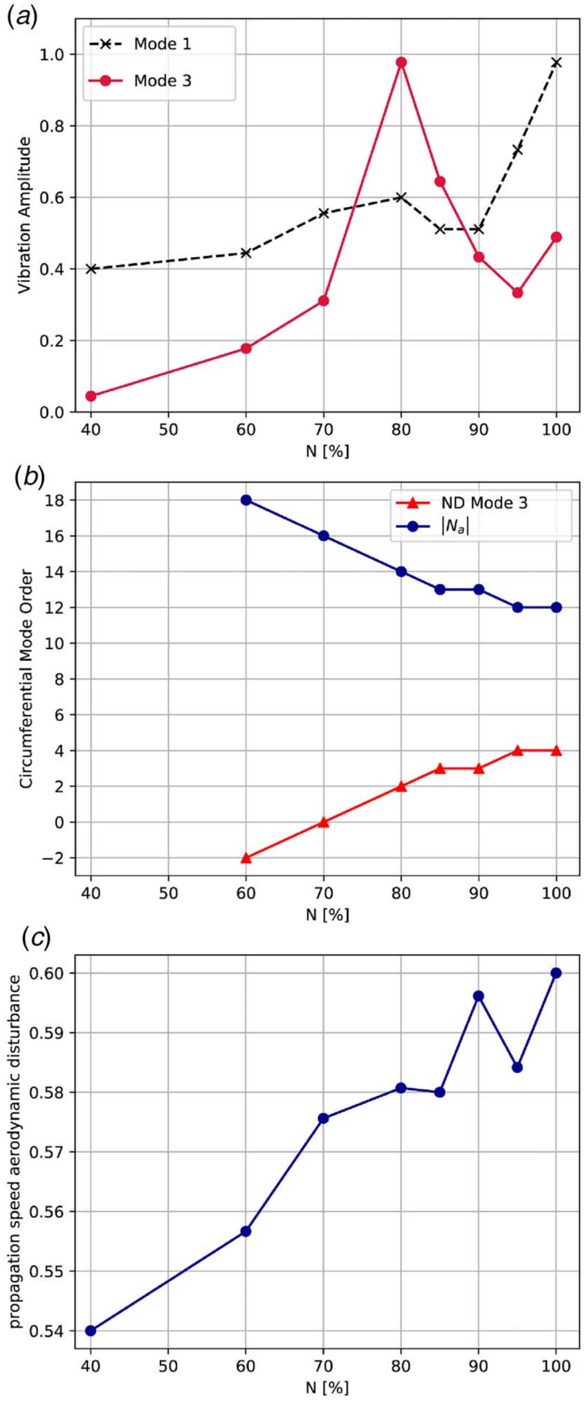

Fig. 19 Observed non-synchronous modes for different speedlines: (*a*) maximum pre-stall amplitude of modes 1 and 3, (*b*) dominant nodal diameters and corresponding wave number of aerodynamic disturbance, and (c) propagation speed of aerodynamic disturbance

Discussion

These results closely resemble those presented in Ref. [10] for a high-pressure compressor. It can hence be derived that this low-speed fan suffers from the same instability mechanism (NSV) that is typically critical for high-speed front-stage compressors. This result is generally surprising due to two facts: (1) for high-pressure compressors, the size of the tip clearance was determined as a dominant factor influencing the tendency toward NSV [25]. In the case of the current investigation, the tip clearance and hub-to-tip ratio are small compared to a typical high-speed compressor. (2) The speedline, at which the NSV amplitude was most significant, is typically critical concerning flutter. At 80% rotor speed, the Eigenfrequency of Mode 1 is approximately EO1.6. This means that for the typical flutter case [5], in which a forward traveling nodal diameter establishes in resonance with an acoustic duct mode, which is cut-on only in the upstream direction, structural Nodal Diameters 2 and 3 fulfill the condition, fitting well into the cases described in the literature. However, no trace of these vibration patterns is observed for the fan under investigation. This result is extremely important for future designs since the investigated fan was particularly designed regarding criteria to avoid flutter, related to acoustic interaction with the machine intake. However, it suffers from another non-synchronous aeroelastic problem which is depending on an aerodynamic convective mechanism. A strong influence of the turbulence model was observed concerning the evolution of the blockage in the tip region. With the $k-\omega$ setup, the performance characteristic and the development of unsteady disturbances upstream of the blockage zone could be reproduced adequately, even though at highly throttled operating points the losses in the rotor tip region are overestimated. With the more stable $k-l$ turbulence model, however, the drop in the performance curve is not predicted coherently with the experiment. All these results clearly indicate that the dominant factor determining both the performance and the instability onset mechanism is the evolution of the tip-leakage flow and its interaction with the shock, typically discussed in the literature under the term vortex breakdown. It is well known that the prediction of this effect strongly depends on the modeling of turbulence. A more detailed study will be carried out in the future to address this topic. Nevertheless, the current setup already predicts the correct propagation speed and intensity of the disturbances and is hence suitable to study the effects leading to NSV. Evidently, the circumferential distribution of disturbances in the simulation is not representative since no blade movement was imposed and periodic boundary conditions are present for a sector of four rotor blades. According to the explanation for the lock-in mechanism, during NSV described by Ref. [9], only the free propagation speed of disturbances and their conservation in the upstream part of the passage is relevant for the evolving vibration pattern. These results clearly indicate that the relevant flow structure which leads to the observed vibrations is captured with the unsteady calculations. It is now envisaged to perform coupled simulations of the 360 setup in order to reproduce the entire interaction phenomenon. The nature of the convected disturbances is a periodic modulation of the aerodynamic field close to the casing. The disturbances are not singular, not necessarily aerodynamically coupled around the circumference [10], and do not result from flow separations [9]. In simulations with preimposed torsional blade oscillation [9], no boundary layer separation was observed but rather distortions of the circulation are periodically shed from the blade boundary layer and convect around the circumference. The convected disturbance of circulation modulates the loading of trailing blades and causes modal forcing, thus triggering NSV. It is hence not a vortex shedding frequency (Strouhal) that dominates the phenomenon but the interaction of blade oscillation and convective propagation of disturbances. The results of the current study confirm the findings presented in Ref. [9].

Conclusion

In the presented study, a composite low-speed fan stage for UHBR applications has been investigated experimentally and numerically. The experiments show a flat performance characteristic with a significant drop of the total pressure ratio toward throttled operating points. The measured radial profiles indicate strong overloading of the rotor tip which could be associated with a breakdown of the tip-leakage vortex. At highly throttled conditions, the rotor develops aerodynamic disturbances which propagate circumferentially between the leading edges upstream of the blockage zone. These disturbances excite structural vibration patterns and lead to a phenomenon that is discussed under the term non-synchronous vibration.

Unsteady measurements clearly revealed the most significant vibration at the 80% speedline, limiting the operating range before the onset of the rotating stall. It was observed that the propagation speed of aerodynamic disturbances remains constant between 55% and 60% of the rotation speed, slightly adapting to the closest matching structural interaction pattern with the third blade eigenmode according to Ref. [9].

A strong influence of the turbulence model has been observed concerning the prediction of the performance characteristic. With a $k-\omega$ setup, adequate results have been obtained, whereas a systematic misprediction of the flow structure close to the casing is still present. However, the evolution and the propagation speed of the disturbances responsible for NSV are well captured in unsteady simulations allowing further studies on the interaction mechanism.

The presented results indicate that despite a lower relative tip clearance, the investigated low-speed fan suffers from instability phenomena which are typical for front-stage high-pressure compressors, dominated by the evolution of the tip-leakage flow. Research efforts will be necessary for the future to accurately understand and predict these phenomena to allow for robust designs. Established procedures to avoid flutter are not suitable to eliminate the observed aeroelastic interaction mechanism.

Furthermore, accurate simulation of the complex flow structure in the tip region will be necessary to allow the prediction of the fan performance, which is evidently not possible with established procedures and particularly turbulence models.

Acknowledgment

The presented research was supported through the European Unions Seventh Framework Programme for research, technological development and demonstration, ENOVAL (Grant No. 604999). Assessment of the test facility was enabled through financial supports of Agence Nationale de la Recherche (ANR, Project EquipEx PHARE) and Conseil pour la Recherche Aeronautique Civile (CORAC—Programme CUMIN). Buildings and infrastructure were supported by Ecole Centrale de Lyon (ECL) and instrumentations supported by Institut Carnot (INGENIERIE@LYON—Project MERIT). Numerical studies were supported by GENCI granting access to CINES through allocation DARI n° A0072A07410. We are grateful for the continuous collaboration and financial support of SAFRAN AE since the beginning of this project and specifically for the present measurement campaign. The authors are particularly grateful for the technical advice of D.Guegan, N.Rochuon, J.Talbotec as well as the precious contributions of Gilbert Halter, Lionel Pierrard, Pierre Laucher, and Sebastien Goguey.

Conflict of Interest

There are no conflicts of interest.

Data Availability Statement

The authors attest that all data for this study are included in the paper. Data provided by a third party are listed in Acknowledgment.

Nomenclature

h = duct height
l = characteristic length of large-scale turbulence
t = time
M = Mach number
R = radius
c_{prop} = propagating speed
N_a = wavenumber (circumferential mode order)
N_b = number of blades
.rel = relative frame of reference
.stat = stationary frame of reference
ADP = aerodynamic design point
Pt = total pressure
Tt = total temperature
Ω = rotor speed
ω = specific dissipation rate

References

[1] Owens, R., Hasel, K., and Mapes, D., 1990, “Ultra High Bypass Turbofan Technologies for the Twenty-First Century,” AIAA 26th Joint Propulsion Conference, Orlando, FL, July 16–18.
[2] Peters, A., Spakovszky, Z. S., Lord, W. K., and Rose, B., 2014, “Ultrashort Nacelles for Low Fan Pressure Ratio Propulsors,” ASME J. Turbomach., **137**(2), p. 021001.
[3] Borradaile, J., 1988, “Towards the Optimum Ducted UHBR Engine,” AIAA 24th Joint Propulsion Conference, Boston, MA, July.
[4] Zhai, Y., Bladh, R., and Dyverfeldt, G., 2012, “Aeroelastic Stability Assessment of an Industrial Compressor Blade Including Mistuning Effects,” ASME J. Turbomach., **134**(6), p. 060903.
[5] Vahdati, M., and Cumpsty, N., 2015, “Aeroelastic Instability in Transonic Fans,” ASME J. Eng. Gas Turbines Power, **138**(2), p. 022604.
[6] Stapelfeldt, S., and Vahdati, M., 2019, “Improving the Flutter Margin of an Unstable Fan Blade,” ASME J. Turbomach., **141**(7), p. 071006.
[7] Kielb, R. E., Barter, J. W., Thomas, J. P., and Hall, K. C., 2003, “Blade Excitation by Aerodynamic Instabilities: A Compressor Blade Study”. ASME Paper No. GT2003-38634.
[8] Kameier, F., and Neise, W., 1997, “Rotating Blade Flow Instability as a Source of Noise in Axial Turbomachines,” J. Sound Vib., **203**(5), pp. 833–853.
[9] Stapelfeldt, S., and Brandstetter, C., 2020, “Non-synchronous Vibration in Axial Compressors: Lock-in Mechanism and Semi-analytical Model,” J. Sound Vib., **488**, p. 115649.
[10] Brandstetter, C., Jungst, M., and Schiffer, H., 2018, “Measurements of Radial Vortices, Spill Forward, and Vortex Breakdown in a Transonic compressor,” ASME J. Turbomach., **140**(6), p. 061004.
[11] Stapelfeldt, S., and Vahdati, M., 2018, “On the Importance of Engine-Representative Models for Fan Flutter Predictions,” ASME J. Turbomach., **140**(8), p. 081005.
[12] Brandstetter, C., Pages, V., Duquesne, P., Paoletti, B., Aubert, S., and Ot- tavy, X., 2019, “Project PHARE-2, A High-Speed UHBR Fan Test Facility for a New Open-Test Case,” ASME J. Turbomach., **141**(10), p. 101004.
[13] Town, J., and Camci, C., 2011, “Sub-miniature Five-Hole Probe Calibration Using a Time Efficient Pitch and Yaw Mechanism and Accuracy Improvements”. ASME Paper No. GT2011-46391.
[14] Gazaix, M., Jolls, A., and Lazareff, M., 2002, “The Elsa Object-Oriented Computational Tool for Industrial Applications”. ONERA Technical Publications, 220.
[15] Smith, B., 1990, “The k-kl Turbulence Model and Wall Layer Model for Compressible Flows,” AIAA 21st Fluid Dynamics, Plasma Dynamics and Lasers Conference, Seattle, WA, June.
[16] Kok, J., 2000, “Resolving the Dependence on Freestream Values for the $k-\omega$ Turbulence Model,” AIAA J., **38**(7), pp. 1292–1295.
[17] Vahdati, M., Sayma, A. I., Freeman, C., and Imregun, M., 2004, “On the Use of Atmospheric Boundary Conditions for Axial-Flow Compressor Stall Simulations,” ASME J. Turbomach., **127**(2), pp. 349–351.
[18] Choi, M., Smith, N., and Vahdati, M., 2013, “Validation of Numerical simulation for Rotating Stall in a Transonic Fan,” ASME J. Turbomach., **135**(2), p. 021004.
[19] Zhao, F., Dodds, J., and Vahdati, M., 2013, “Poststall Behaviour of a Multi-stage High Speed Compressor at Off-Design Conditions,” ASME J. Turbomach., **140**(12), p. 121002.

[20] Zhang, W., and Vahdati, M., 2020, “Stall and Recovery Process of a Transonic Fan With and Without Inlet Distortion,” ASME J. Turbomach., **142**(1), p. 011003.

[21] Lu, Y., Lad, B., Green, J., Stapelfeldt, S., and Vahdati, M., 2019, “Effect of Geometry Variability on Transonic Fan Blade Untwist,” Int. J. Turbomach. Propuls. Power, **4**(3), p. 24.

[22] Schlechtriem, S., and Ltzerich, M., 1997, “Breakdown of Tip Leakage Vortices in Compressors at Flow Conditions Close to Stall,” ASME Paper No. 97-GT-041.

[23] Furukawa, M., Inoue, M., Saiki, K., and Yamada, K., “The Role of Tip Leakage Vortex Breakdown in Compressor Rotor Aerodynamics,” ASME J. Turbomach., **121**(3), pp. 469–480.

[24] Brandstetter, C., Paoletti, B., and Ottavy, X., 2019, “Compressible Modal Instability Onset in an Aerodynamically Mistuned Transonic Fan,” ASME J. Turbomach., **141**(3), p. 031004.

[25] Hah, C., 2017, “Effects of Double-Leakage tip Clearance Flow on the Performance of a Compressor Stage With a Large Rotor tip gap,” ASME J. Turbomach., **139**(6), p. 061006.